

1 Mapping irregularities in the postsunset equatorial 2 ionosphere with a network of HF beacons

3 **D. L. Hysell¹***, E. Rojas¹, H. Goldberg¹, M. A. Milla², K. Kuyeng²,
4 A. Valdez², Y. T. Morton³, and H. Bourne³

5 ¹Earth and Atmospheric Sciences, Cornell University

6 ²Radio Observatorio de Jicamarca, Institute Geofísico del Peru

7 ³Aerospace Engineering Sciences Department, University of Colorado Boulder

8 ¹Ithaca, NY, USA

9 ²Lima, Peru

10 ³Boulder, CO, USA

11 **Key Points:**

- 12 • An HF beacon network has been deployed in Peru for inferring ionospheric elec-
tron number densities regionally.
- 13 • Sensitivity analysis and absorption computation turn signal power into additional,
useful observable.
- 14 • Regional electron density data can be combined with incoherent scatter radar mea-
surements for studying and forecasting space weather.

*3114 Snee Hall, Cornell University, Ithaca, NY 14853 USA

Corresponding author: D. L. Hysell, david.hysell@cornell.edu

18 **Abstract**

19 Data from a network of high-frequency (HF) beacons deployed in Peru are used
 20 to estimate the regional ionospheric electron density in a volume. Pseudorange, accu-
 21 mulated carrier phase, and signal power measurements for each of the 36 ray paths pro-
 22 vided by the network at a 1-min. cadence are incorporated in the estimates. Additional
 23 data from the Jicamarca incoherent scatter radar, the Jicamarca sounder, and GPS re-
 24 ceivers can also be incorporated. The electron density model is estimated as the solu-
 25 tion to a global optimization problem that uses ray tracing in the forward model. The
 26 electron density is parametrized in terms of B-splines in the horizontal direction and gen-
 27 eralized Chapman functions or related functions in the vertical. Variational sensitivity
 28 analysis has been added to the method to allow for the utilization of the signal power
 29 observable which gives additional information about the morphology of the bottomside
 30 F region as well as absorption including absorption in the D and E regions. The goal of
 31 the effort is to provide contextual information for improving numerical forecasts of plasma
 32 interchange instabilities in the postsunset F region ionosphere associated with equato-
 33 rial spread F (ESF). Data from two ESF campaigns are presented. In one experiment,
 34 the HF data revealed the presence of a large-scale bottomside deformation that seems
 35 to have led to instability under otherwise inauspicious conditions. In another experiment,
 36 gradual variations in HF signal power were found to be related to the varying shape of
 37 the bottomside F layer.

38 **1 Background and motivation**

39 One of the most common manifestations of space weather is the spontaneous gen-
 40 eration of broadband plasma density irregularities in the postsunset equatorial F -region
 41 ionosphere. The phenomenon, often referred to as equatorial spread F (ESF) because
 42 of the spreading it produces in ionogram traces (Booker & Wells, 1938), is attributed to
 43 interchange instability in the F region which can become unstably stratified with the ces-
 44 sation of photoionization. The connection between ESF and interchange instabilities was
 45 established by Woodman and La Hoz (1976) who were the first to render coherent backscat-
 46 ter radar profiles observed at the Jicamarca Radio Observatory in range-time-intensity
 47 (RTI) image format. Their images resembled numerical simulations of interchange in-
 48 stabilities in barium clouds (e.g., Ossakow (1981)). Earlier, working also at Jicamarca,
 49 Farley et al. (1970) had established a causal relationship between the height of the F layer

50 at sunset and the occurrence probability of ESF, a finding which is consistent with if not
51 uniquely indicative of interchange instability. Later, true images of large-scale irregularities
52 associated with ESF were observed with the ALTAIR radar on Kwajalein which
53 can scan from horizon to horizon (Tsunoda et al., 1979). These, together with increas-
54 ingly accurate and finely resolved numerical simulations, cemented the link between ESF
55 and ionospheric interchange instability (see e.g., Keskinen et al. (1980); Zalesak et al.
56 (1982); Zargham and Seyler (1989); Zalesak et al. (1990); Keskinen and Vadas (2009);
57 Krall et al. (2009); Aveiro et al. (2011); Yokoyama et al. (2014)).

58 Forecasting ESF has become imperative because of the hazard it poses to vital ra-
59 dio communication, navigation, and imaging systems which can be degraded by the deep
60 plasma density irregularities ESF produces. However, reliable forecasts of ESF, which
61 exhibits considerable day-to-day variability, have been elusive. Assuming that the physics
62 of plasma interchange instabilities is sufficiently well understood, there are three pos-
63 sible explanations. First, the system could be chaotic. This seems unlikely; in the col-
64 lisional regime where most ESF takes place, the system is not turbulent, and the most
65 important nonlinearity in the governing equations is associated mainly with plasma steep-
66 ening (Zargham & Seyler, 1987, 1989). Second, the most important drivers, the back-
67 ground electric fields and winds, may be inadequately specified. This possibility was ad-
68 dressed in a series of studies at Jicamarca (see Hysell et al. (2015) and references therein).
69 In these studies, the occurrence and non-occurrence of irregularities in the postsunset
70 sector was reproduced in most cases in simulations using drivers inferred from Jicamarca
71 incoherent scatter measurements. The ‘forecasts’ were not entirely accurate, however,
72 as the simulations failed to predict the occurrence of irregularities in a few instances.

73 This finding points to a third explanation which is inadequately specified initial con-
74 ditions. Results from a recent sounding rocket campaign from Kwajalein point to the
75 existence of subtle, large-scale fluctuations in the bottomside F region at sunset which
76 can influence the morphology of the irregularities that form later (Hysell et al., 2020).
77 The fluctuations, which were identified previously by Tsunoda et al. (2010), seem to be
78 too large in scale to be produced purely by plasma processes and may be indicative of
79 neutral waves in the thermosphere or lower thermosphere, a subject which has received
80 considerable attention in the literature (e.g., Kelley et al. (1981); Röttger (1981); Huang
81 et al. (1994); Singh et al. (1997); Keskinen and Vadas (2009); Abdu et al. (2009); Tsun-
82 oda (2010); Taori et al. (2011); Krall et al. (2013)).

83 Here, we explore the possibility of establishing the initial conditions for forecast
 84 simulations of ESF using information derived from HF beacons. A network of HF bea-
 85 con transmitters and receivers has been established around the Jicamarca Radio Obser-
 86 vatory for this purpose. The observables derived from the beacon data include the pseu-
 87 dorange, the Doppler shift or beat carrier phase, the signal power, and the received bear-
 88 ing with the application of interferometry. The goal is to estimate the electron density
 89 in an ionospheric volume surrounding Jicamarca from which to derive initial conditions
 90 for ESF simulations.

91 Below, we discuss the methods used to estimate electron number densities from bea-
 92 con data. We demonstrate the methods with sample data collected in 2019. The role of
 93 the beacon data in an ESF forecast strategy is then described.

94 2 Methods

95 Estimating ionospheric parameters from HF radio measurements is an inverse prob-
 96 lem rooted in control theory and constrained PDE optimization. We consider the limit
 97 of geometric optics where the radio signals are described by rays. The rays are governed
 98 by Fermat’s principle which demands that the phase integral over a ray path with fixed
 99 boundaries be stationary. Here, the boundaries are set by the transmitter and receiver
 100 locations. The constraint comes from the dispersion relation obeyed by the wave in the
 101 medium it occupies. Finding the rays which satisfy the boundary conditions and repro-
 102 duce measurements is an optimization problem.

103 Raytracing can be performed using direct variational methods and numerical re-
 104 laxation. An example of this approach is given by Coleman (2011). Another approach
 105 involves converting the variational problem into a system of coupled first-order differ-
 106 ential equations using the principles of analytic mechanics (e.g. Landau and Lifshitz (1976)).
 107 The result are Hamilton’s equations which describe the evolution of the generalized ray
 108 position $\mathbf{x} \in \mathbb{R}^3$ and its conjugate generalized momentum $\mathbf{p} \in \mathbb{R}^3$ in terms of a Hamil-
 109 tonian $H(\mathbf{x}, \mathbf{p}, \omega, t)$. The momentum and the wave vector \mathbf{k} are related through a met-
 110 ric tensor that depends on the coordinate system in use.

111 Hamilton’s equations are solved using numerical quadrature (ray shooting). It is
 112 generally desirable to compute not only the state parameters \mathbf{x} and \mathbf{k} along the ray but
 113 also their sensitivity to one or more control parameters. This is required both for con-

114 straining the endpoints of the rays and for focusing (see below). Sensitivity analysis can
 115 be performed at first or second order where the gradient and the Hessian of the state pa-
 116 rameters with respect to the control parameters are found, respectively. The problem
 117 is simplified if the control parameters are just the ray initial conditions. For a general
 118 review of sensitivity analysis, see Cacuci et al. (1980).

119 A number of approaches to sensitivity analysis have been developed. One is the
 120 brute-force method in which perturbations are introduced in the initial conditions for
 121 ray shooting and finite differences are applied to the results. The advantage of this ap-
 122 proach is coding simplicity. The main disadvantage is accuracy; large perturbations are
 123 subject to quantization error, and small perturbations to roundoff error. A second ap-
 124 proach is the direct variational method in which the differential equations describing the
 125 control-vector sensitivities are derived and integrated alongside the original raytracing
 126 equations (Nickisch, 1988; Sambridge & Kennett, 1990; Västberg & Lundborg, 1996).
 127 This approach is practical so long as the number of control parameters involved is small.
 128 (A variant of the approach involves solving the sensitivity equations using the method
 129 of Green's functions which may be more numerically efficient in cases where the num-
 130 ber of control parameters is large (Hwang et al., 1978)).

131 Another approach is the adjoint method which is a key tool in data assimilation
 132 (Cao et al., 2003; Tromp et al., 2005). The adjoint method yields sensitivity equations
 133 which may be more expedient to compute given a large number of control parameters.
 134 Consider a Lagrangian function that combines an objective function (which measures
 135 mismatches in the boundary conditions for the ray) with the constraint equation (Hamil-
 136 ton's equations, each multiplied by a Lagrange multiplier). Differentiating the Lagrangian
 137 with respect to the control variables yields, after some manipulation, two new equations.
 138 One is the desired sensitivity equation, and the other is the adjoint equation. The ad-
 139 joint equation will be formally similar to the original constraint equation except with the
 140 Lagrange multipliers replacing the original state variables. Crucially, it may be no harder
 141 to integrate (along ray paths) than the original constraint equation. The analysis pro-
 142 ceeds as follows. 1) Integration of the original constraint equations takes place in the for-
 143 ward direction as usual. 2) Integration of the adjoint equation takes place in the back-
 144 ward direction. 3) The results are used to calculate the sensitivities with one final path
 145 integration. Note that the adjoint problem can be applied not just to fixing ray endpoints

146 and focusing but to the larger problem of adjusting ionospheric model parameters for
 147 optimal congruence with the experimental observables (e.g. M. Psiaki (2019)).

148 A final means of sensitivity analysis is automatic differentiation (e.g. Bartholomew-
 149 Biggs et al. (2000)). We can recognize that computing the right side of Hamilton's equa-
 150 tions (e.g. see Eq. A1) involves a well-defined sequential set of elementary numerical op-
 151 erations. Using nothing more than the exhaustive application of the chain rule, the sen-
 152 sitivities of the state parameters to perturbations can be computed to machine precision
 153 by a suitable algorithm. Automatic differentiation therefore obviates the need for po-
 154 tentially tedious manual calculations required by the direct and adjoint methods. It has
 155 become the cornerstone for constructing neural networks.

156 The work described here makes use of direct variational sensitivity analysis for ray-
 157 tracing and is posed in spherical coordinates. We consider an inhomogeneous, birefrin-
 158 gent, lossy ionospheric plasma with a maximum usable frequency (MUF) greater than
 159 the beacon frequencies. Details regarding the formulation of the problem and the sen-
 160 sitivity analysis in particular are provide in the appendix. Some additional modeling de-
 161 tails are described below.

162 2.1 Signal power and focusing

163 The power of the received signal depends on a number of factors to be addressed
 164 here and later in the paper. One is the power delivered by the transmitting antenna into
 165 the radiative flux tube that terminates at the receiver. Formally, this is $P_\Omega d\Omega$ where P_Ω
 166 is the power transmitted per unit solid angle and $d\Omega$ is the differential solid angle of the
 167 flux tube. The result depends on the known transmitter power and antenna radiation
 168 pattern and on the transmit ray bearing which is estimated in the course of the raytrac-
 169 ing analysis.

170 Another factor is absorption. So long as the imaginary part of the index of refrac-
 171 tion remains small compared to the real part along the ray path, the absorption can be
 172 calculated using an elementary, approximate formula which is integrated with the oth-
 173 ers during ray tracing with little added computational cost (Jones & Stephenson, 1975).
 174 The result depends on the electron collision frequency model used (see below) and on
 175 the electron number density profile, mainly at altitudes where collisions are frequent. Power
 176 measurements can thereby be used to diagnose the state of the *D* and *E* regions, where

177 inelastic electron-neutral collision frequencies are large even where the electron number
 178 density is comparatively small.

179 The third factor is the cross-sectional area of the flux tube at the receive site. Es-
 180 timating this area is referred to as focusing (e.g. Nickisch (1988); Budden (1991); Västberg
 181 and Lundborg (1996)). Consider a radiative flux tube at the transmitter with a differ-
 182 ential solid angle $d\Omega = \sin(\eta_t)d\eta_t d\xi_t$ where $d\xi_t$ and $d\eta_t$ are variations in the azimuth
 183 and zenith angle of the transmit ray bearing, respectively. The corresponding differen-
 184 tial cross-sectional area of the tube at the receive antenna will be

$$dA = R^2 \cos(\eta_r) \sin(\theta) \left| \frac{\partial \theta}{\partial \eta_t} \frac{\partial \phi}{\partial \xi_t} - \frac{\partial \theta}{\partial \xi_t} \frac{\partial \phi}{\partial \eta_t} \right| d\eta_t d\xi_t \quad (1)$$

185 where θ and ϕ represent colatitude and longitude, respectively, R is the radial distance
 186 from the center of the earth, and η_r is the receive zenith angle. The partial derivatives
 187 in Eq. 1 must be determined through sensitivity analysis. The analysis is expected to
 188 hold except near a caustic where dA vanishes and the geometric-optics limit breaks down.

189 Neglecting absorption, the predicted power to the receiver will be the product of
 190 the quotient $P_\Omega d\Omega/dA$ and the receive antenna effective aperture along the bearing of
 191 the incoming ray which is also known. Including absorption, it becomes possible to pre-
 192 dict power measurements for the rays and to penalize features in the electron density
 193 model giving rise to discrepancies. Like the pseudorange and beat carrier phase observ-
 194 ables, the power observables are enter into the optimization objective functions through
 195 least-squares operators.

196 2.2 Electron collision model

197 A detailed analysis of ionospheric absorption and the underlying treatment of elec-
 198 tron collisions was presented recently by Zawdie et al. (2017) who summarized practices
 199 over the last several decades. They distinguished between deviative absorption which oc-
 200 curs near the reflection height where rays bend drastically and non-deviative absorption
 201 which occurs well below the reflection height where rays are nearly straight but where
 202 the product of the electron number density and collision frequency can be much greater.
 203 Whereas the former is relatively consistent and relatively minor for rays that penetrate
 204 to the F region, the latter is more variable (occurring only when D and/or E layers are
 205 present) and can be much larger. For the present purposes, we neglect contributions from

206 deviative absorption and concentrate on non-deviative absorption. We consequently ne-
 207 glect electron Coulomb collisions and consider only electron-neutral collisions.

208 Zawdie et al. (2017) point out that two formulations of the dispersion relation for
 209 ionospheric waves are in common use – the Appleton Hartree formula (Budden, 1985)
 210 and the Sen Wyller formula (Sen & Wyller, 1960). Whereas the former is a cold-plasma
 211 approximation, the latter assumes the collision frequency varies with electron energy. The
 212 former incorporates an effective collision frequency which is the monoenergetic collision
 213 frequency integrated over the electron thermal distribution. The latter incorporates the
 214 monoenergetic frequency evaluated at the most likely electron velocity (and is only de-
 215 fined for electron-neutral collisions). The collision frequency values to be used with the
 216 two formulations therefore differ. Zawdie et al. (2017) concluded that the two formula-
 217 tions predict comparable absorption rates in the *D* and *E* regions if the Appleton Hartree
 218 formula is populated with the effective collision frequency as defined, for example, by Schunk
 219 and Nagy (2009).

220 Below 150–200 km altitude, the most important electron neutral momentum trans-
 221 fer collisions are with molecular nitrogen and molecular oxygen with rates that depend
 222 on the density of each species along with the electron temperature. Collisions with atomic
 223 oxygen become increasingly important with increasing altitude. The effective electron
 224 neutral collision frequency can be calculated using neutral densities taken from the NRLM-
 225 SISE00 empirical model and the formulas provided by Schunk and Nagy (2009). The re-
 226 sult can be represented accurately by a simple bi-exponential function (e.g. Settimi et
 227 al. (2015)). A bi-exponential electron-neutral collision frequency calculated for the ap-
 228 propriate latitude, longitude, local time sector, and F10.7 cm solar flux level is used for
 229 our analysis.

230 2.3 Electron density profile shapes

231 A simple parametrization of the electron density profile is required for the forward
 232 model. Chapman profiles are a natural choice, being the foundation for analytic solu-
 233 tions of actual profile shapes under certain simplifying assumptions. The Chapman pro-
 234 file is defined by four parameters: the peak electron number density, the peak height,
 235 and the scale height which can differ in the bottomside and topside. Chapman profiles
 236 could be superimposed to represent multiple ionospheric layers

Studies have pointed to other parametrizations which can reproduce actual ionospheric density profiles with smaller residuals, however. Nava et al. (2008) discuss parametrizations based on semi-Epstein layers which are also defined by a peak number density, peak height, and distinct bottomside and topside scale-height controls. An important distinction is that the topside scale height varies in a prescribed way.

Either Chapman or semi-Epstein layers can be used in the existing forward model. In this study, we describe the *F* region with a four-parameter Chapman layer. The model also has the provision to add an *E* layer with a Chapman or semi-Epstein layer with one free parameter, the peak density. This is a reasonable simplification given that the shape of the equatorial *E* layer has been found to be relatively invariant (Hysell & Chau, 2001). In the interest of simplification, there is no *E* layer in this study, however.

The model also has provisions for a simple *D* layer which should sometimes be detectable in the signal power observable at twilight. Cummer et al. (1998) present a two-parameter *D*-region parametrization that could be added with relatively light additional computational burden. A four-parameter model developed by McCormick (2019) improves upon the two-parameter model by representing the split that occurs in the daytime. The computational burden of the improved model is significantly higher, however. For this study, we use incorporate a simple Gaussian layer with a five-kilometer half width and a peak height of 85 km.

2.4 B-spline horizontal interpolation

The electron number density model is extended to three dimensions with the use of B-splines (e.g. De-Boor (1978)) in the manner outlined by M. L. Psiaki et al. (2015). The five coefficients defining the aforementioned profile shapes are each expanded in the form of either bicubic or biquintic B-splines. These are families of polynomials with weights that are prescribed at certain nodes on a grid. B-splines of degree n have continuous derivatives through $n-1$. The functions and their first and second derivatives are tabulated within the algorithm. We use a two-dimensional grid in latitude and longitude with uniformly spaced nodes spanning the region where the beacons are deployed. The work presented here makes use of biquintic B-splines on a 15×15 grid, implying a total of 1125 parameters.

267 **2.5 Numerical quadrature**

268 The sensitivity equations are stiffer than the ordinary raytracing equations. Whereas
 269 any number of quadrature methods would be suitable for integrating the latter, includ-
 270 ing adaptive methods, the former require methods specially designed to handle stiff sys-
 271 tems. Here, we utilize an extrapolation method based on the linearly implicit midpoint
 272 rule of Bader-Dueflhard described by Hairer and Wanner (1990).

273 **2.6 Objective function**

274 The optimization routine minimizes in the least-squares sense an objective func-
 275 tion composed of a number of penalties. The penalties include discrepancies between model
 276 predictions and experimental observables from the HF network, the group delay, accu-
 277 mulated Doppler phase, and power, namely. Given three transmitters, six receivers, and
 278 two frequencies, there are thirty-six rays and 108 penalties to consider here.

279 Additional penalties are derived from electron density profiles measured by the Ji-
 280 camarca incoherent scatter radar or the ionosonde and from TEC measurements made
 281 by GNSS receivers deployed regionally.

282 The objective function also includes penalties used to introduce regularization. The
 283 electron density model is mixed determined and poorly conditioned, and regularization
 284 is required for stability. We penalize the curvature in the horizontal direction of the five
 285 parameters that control the electron density representation. This prevents the produc-
 286 tion of spurious model features lacking support in the data.

287 The objective function is minimized using a Levenberg Marquardt algorithm. The
 288 computation is parallelized, with raytracing for each ray handled by a separate proces-
 289 sor. Ray shooting also takes place within a Levenberg Marquardt algorithm with the Ja-
 290 cobian matrix supplied through sensitivity analysis.

291 **3 Data presentation**

292 An HF beacon network consisting of three transmit and six receive stations has been
 293 deployed in Peru in the vicinity of the Jicamarca Radio Observatory for specifying the
 294 ionospheric electron density regionally with the goal of forecasting plasma instability as-
 295 sociated with equatorial spread *F* (ESF). The transmitters operate at two frequencies,

296 2.72 MHz and 3.64 MHz, and utilize distinct pseudorandom codes with baud widths of
 297 $10 \mu\text{s}$ and repetition times of 0.1 s, giving a compression ratio of 10,000. The transmitter
 298 power is approximately 10 W. Dipole antennas are used for transmission and reception.
 299 The observables from the receivers include pseudorange, Doppler shift or accumulated
 300 carrier phase, and power at a cadence of once per minute. Technical details regarding
 301 the network were given by Hysell et al. (2018). The locations of the transmitters and
 302 receivers are shown in Table 1.

station	latitude (north)	longitude (east)	altitude (masl)
Jicamarca	-11.950	-76.873	52
Huancayo	-12.042	-75.323	3119
Mala	-12.666	-76.628	31
La Merced	-11.126	-75.368	817
Barranca	-10.760	-77.760	55
Oroya	-11.551	-75.942	3790
<hr/>			
Ancon	-11.777	-77.150	51
Sicaya	-12.040	-75.296	3330
Ica	-14.089	-75.736	402

Table 1. HF beacon station locations. Receive (transmit) stations are above (below) the line.

303 We present data from two nights of observation. The first night is June 10, 2019.
 304 ESF occurs rarely in the postsunset interval in the Peruvian sector in June and did not
 305 occur in the interval of interest here between 1900-2200 LT. It did occur later, near mid-
 306 night, as is common during periods of very low solar flux.

307 The motivation for examining these particular data is evident in Fig. 1 which shows
 308 pseudorange and accumulated carrier phase data for all 18 3.64-MHz ray paths covered
 309 by the network. Our convention is to define the pseudorange as $c\tau/2$ where τ is the time
 310 of flight of the signal. The accumulated Doppler phase is the time integral of the Doppler
 311 velocity in m/s, $v = \omega/k$, where ω is the Doppler frequency and k is the scattering wavenumber
 312 ($4\pi/\lambda$). An arbitrary offset is added to the accumulated carrier phase so that the
 313 curves can be plotted on the same axes as the pseudorange.

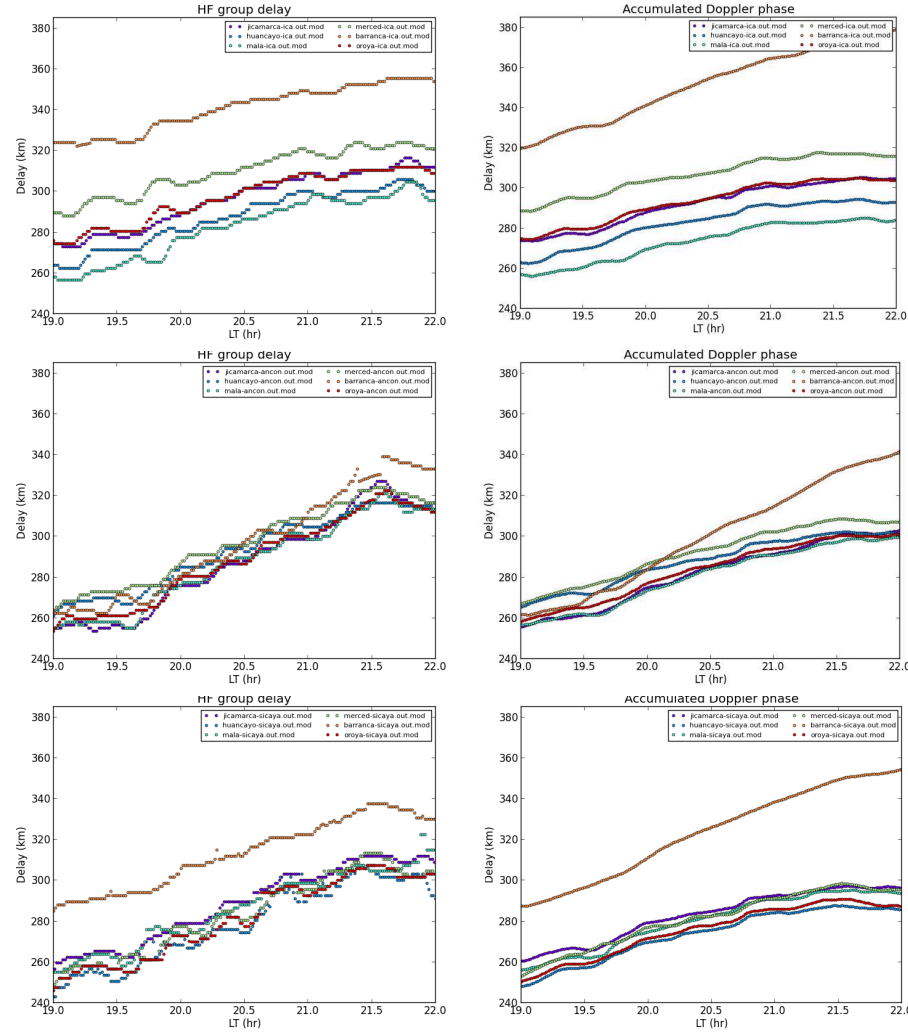


Figure 1. Group delay (left) and accumulated carrier phase (right) measurements vs. local time on June 10, 2019 for 3.64 MHz. The top, middle, and bottom rows represent signals transmitted from Ica, Ancon, and Sicaya, respectively. The six curves in each panel represent signals received at six different receive sites as indicated.

314 The figure depicts a gradual increase in pseudorange and accumulated carrier phase
 315 for all the ray paths after 1900 LT. This is a common feature of data from the network
 316 and reflects the rise of the postsunset *F* layer due to a combination of proper motion and
 317 recombination. More remarkable are the unusually distinct quasi-periodic variations in
 318 all the curves. The variations have periods of 20–30 min. and may be indicative of medium-
 319 scale traveling ionospheric disturbances (MSTIDs). Capturing them in numerical sim-
 320 ulations could be an important part of an ESF forecast strategy.

321 Similar variations are not clearly evident in the HF data for 2.72 MHz (not shown).
 322 They are likewise not especially clear in the signals from the transmitter at Ica. Ica is
 323 the southernmost station in the network and the transmitter most distant from the re-
 324 ceivers. The variations are more distinct in the signals transmitted from Ancon and Sicaya
 325 which involve shorter, higher elevation paths. Overall, the rays with the highest turn-
 326 ing points are the ones with the strongest quasiperiodic variations. The variations are
 327 furthermore much more distinct in the pseudorange observables than in accumulated car-
 328 rier phase. That the phases of the fluctuations in different ray paths can differ indicates
 329 that their dominant physical scale sizes are not very long compared to the distances be-
 330 tween the stations. That the amplitudes and periods of the fluctuations vary in time and
 331 between ray paths argues that one or more wave packets as opposed to a single, coher-
 332 ent, monochromatic wave were at work.

333 The Jicamarca incoherent scatter radar was not operating on June 10, 2019. Data
 334 from the Jicamarca ionosonde are available for supplementing the HF data, however. Also
 335 available are TEC estimates from a GNSS receiver deployed at Jicamarca by the Satel-
 336 lite Navigation and Sensing (SeNSe) Laboratory at the University of Colorado Boulder.
 337 The TEC data were derived using an algorithm which simultaneously estimates the TEC
 338 and receiver hardware bias based on measurements from a single receiver Bourne (2016);
 339 Bourne et al. (2016).

340 Fig. 2 depicts the volumetric electron density reconstructed in the Peruvian sec-
 341 tor from the HF pseudorange and Doppler-shift data together with GPS measurements
 342 and soundings at 15-min intervals from the ionosonde at Jicamarca. The figure shows
 343 isodensity contours for 10^{10} and 10^{11} m^{-3} , respectively. The cadence for the method is
 344 once per min, and reconstructions are shown here at 30-min intervals.

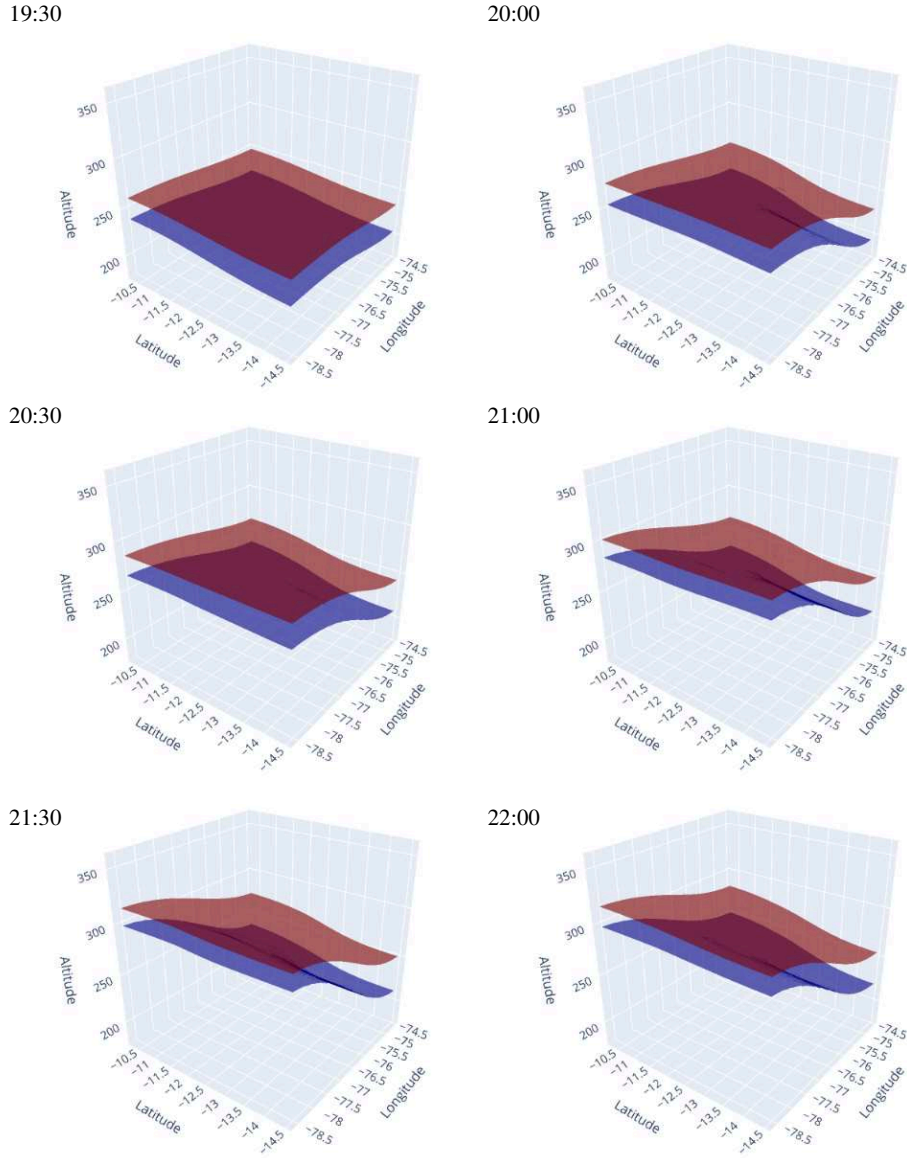


Figure 2. Reconstructed electron density isosurfaces generated from HF pseudorange and Doppler-shift data over a period of three hours on June 10, 2019. The blue (red) surfaces represent $N_e = 1 \times 10^{10}$ and $1 \times 10^{11} \text{ m}^{-3}$, respectively.

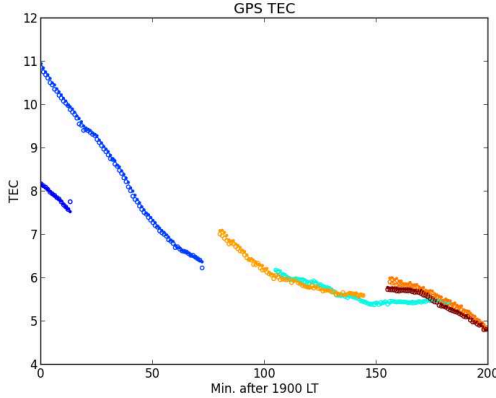


Figure 3. Figure showing measured (open circles) and modeled (closed circles) GPS TEC values for six PRNs passing through the region. Different colors are assigned to different PRNs.

Three main features are evident in the reconstructions. First, the bottomside F layer is seen to ascend slowly throughout the interval. Second, there is a modest meridional tilt in the isosurfaces which could be telltale of the development of the Appleton anomaly to the south of the dip equator which is at approximately -12° latitude. Third, a distinct zonal tilt on the layer height emerges during the interval shown. The tilt could be the result of local convection or the advection of a deformed bottomside through the field of view. Radar data from Jicamarca shown below will be suggestive of the latter scenario.

GPS-TEC measurements from a receiver at Jicamarca were incorporated in the electron density recovery algorithm. TEC estimates are computed from the electron density model by integrating along the bearing to the satellite. Model-data discrepancies are then incorporated in the global optimization problem. Only PRNs with elevation angles greater than 60° were considered, and then no more than three PRNs at any given time. Fig. 3 shows a comparison between the GPS measurements (open circles) and model predictions (closed circles), with different colors assigned to different PRNs. As GPS TEC offers the only constraint on the model topside ionosphere scale height in this case, the good agreement merely means that the topside scale height estimates could be fairly uniform across the region while maintaining consistency with the satellite data.

In addition to the coarse structure evident in Fig. 2, the HF reconstruction method can also capture relatively fine structure in the electron density. We show this by inspecting the shapes of isodensity curves calculated at different times. Fig. 4 shows the rela-

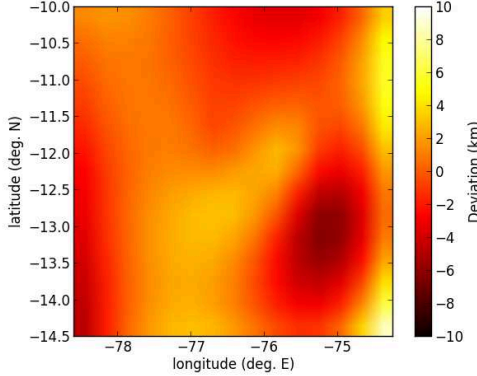


Figure 4. Fine structure in reconstructed electron isodensity surface height at 1950 LT (see text).

365 tive vertical displacements of the $N_e = 10^{11} \text{ m}^{-3}$ isosurface. Before plotting, we fit and
 366 subtracted the quadratic trend in the surface height to remove as much of the gross struc-
 367 ture already evident in Fig. 2 as possible. The result shows residual wavelike variations
 368 in layer height across the region. The variations are mainly zonal but also partly merid-
 369 ional.

370 Over time, the features seen in Fig. 4 propagate slowly to the east for a time be-
 371 fore coming to rest. The amplitude of the features, as measured by the difference between
 372 the highest crest and lowest trough, varies periodically, however. The period is approx-
 373 imately 30 min. Fig. 4 was computed at 1950 LT when the amplitude was a maximum.
 374 The periodicity is similar to that seen in the raw data in Fig. 1. Overall, the model sug-
 375 gests the presence of spatial fluctuations in layer height which are not propagating but
 376 which are waxing and waning periodically. Changes in layer height cause variations in
 377 the pseudoranges of the rays mainly by inducing tilts away from great-circle paths.

378 The JULIA coherent scatter radar at Jicamarca was operating on June 10, 2019,
 379 and the observations are represented in range-time-intensity (RTI) format in Fig. 5. The
 380 brightness of the image pixels is proportional to the signal-to-noise ratio on a dB scale.
 381 The hue represents Doppler shift, with blue (red) tones implying motion toward (away
 382 from) the radar on a scale spanning $\pm 100 \text{ m/s}$. The saturation of the pixels represents
 383 Doppler width, with pure (pastel) colors signifying narrow (wide) spectra.

2019/06/10 22:17:29

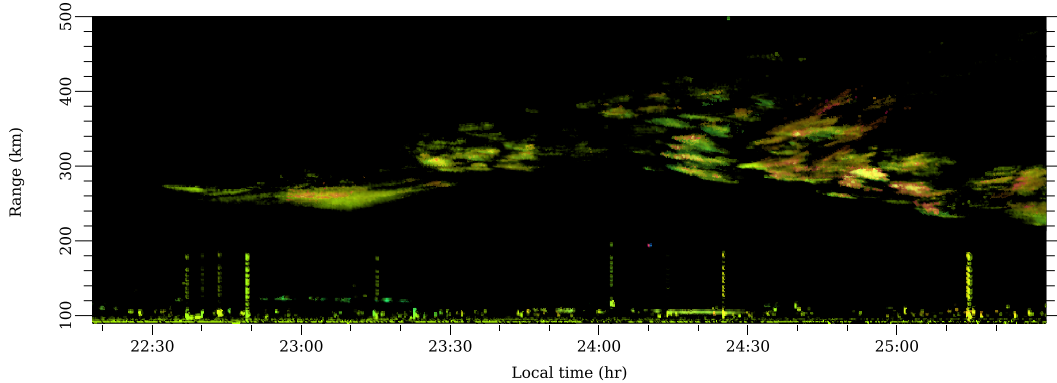


Figure 5. Jicamarca RTI representation of coherent scatter from ESF irregularities observed on June 10, 2019.

384 Fig. 5 is typical in some respects for ESF events observed at Jicamarca. A narrow
 385 bottom-type scattering layer at about 250 km altitude evolved after about 2330 LT into
 386 a series of vertical plumes characteristic of plasma interchange instability. Results from
 387 interferometry and radar imaging (now shown) indicate that the flow was mainly east-
 388 ward over the radar during the event, although shears were sometimes present, and the
 389 bottom-type layer drifted very slowly.

390 The most remarkable aspects of the ESF event were its occurrence in June, an un-
 391 favorable season for ESF in the Peruvian sector, and its late onset time, which was well
 392 after sunset. The HF electron density reconstructions suggest a scenario in which a large-
 393 scale bottomside deformation advected over the radar, causing the layer to appear to
 394 rise, plateau, and then fall overhead. Such a deformation would be conducive to iono-
 395 spheric interchange instability, which has a growth rate that increases with altitude, and
 396 to the clustering of irregularities in the vicinity of the deformation (Hysell et al., 2020).
 397 Additionally, the fine structure evident in Fig. 4 could be interpreted either as a seed for
 398 instability or evidence of instability underway.

399 The next dataset considered here is from Dec. 3, 2019. The JULIA RTI plot for
 400 the event is shown in Fig. 6. This event was characterized by a narrow bottom-type scat-
 401 tering layer emerging at 2000 LT that turned to a more vertically-developed bottomside
 402 layer at about 2130 and then a small topside radar plume that passed overhead at about
 403 2330 LT.

Tue Dec 3 19:04:43 2019

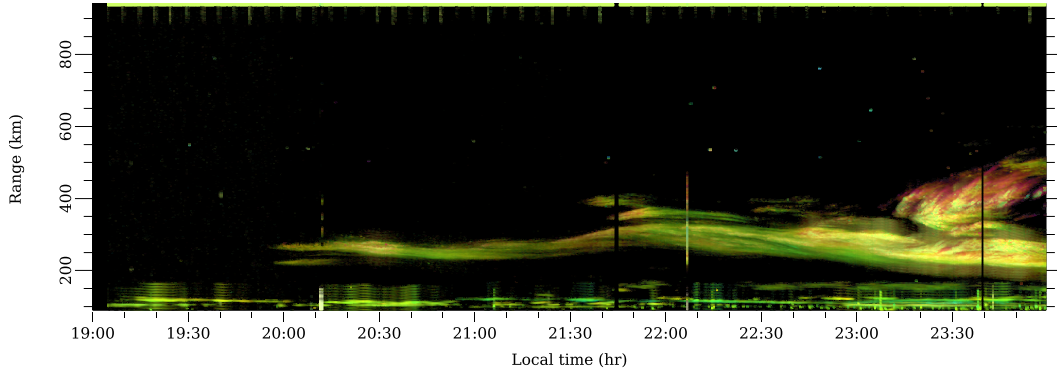


Figure 6. Jicamarca RTI representation of coherent scatter from ESF irregularities observed on Dec. 3, 2019.

404 The Jicamarca incoherent scatter radar reported very small vertical plasma drifts
 405 prior to 2000 LT and no prereversal enhancement. Starting at 2000 LT, the drifts be-
 406 gan increasing approximately linearly, reaching about 10 m/s by 2130 LT by the time
 407 small plumes began passing over the radar. Zonal Pedersen currents associated with ver-
 408 tical drifts are the main drivers for the collisional interchange instability. The small plumes
 409 are likely a direct consequence of the late ascent of the layer.

410 A very atypical aspect of the Dec. 3, 2019, event was the brief appearance of co-
 411 herent scatter just above the F peak between about 1800–1830 LT in the ISR data (not
 412 shown). This was a rare example of so-called “daytime spread F ” which was described
 413 by Chau and Woodman (2001). The phenomenon contaminated the incoherent scatter
 414 observations along with the HF. We avoid contamination from the daytime spread F echoes
 415 by considering HF data from after 1845 LT.

416 The pseudorange and carrier phase data for the Dec. 3, 2019 event were qualita-
 417 tively similar to those from June 10, 2019, only with more modest quasiperiodic vari-
 418 ations and with smaller increasing trends between about 1845–2030 LT. In addition to
 419 these observables, the relative power associate with the first hops for all the links in the
 420 Dec. 3 HF data was also calculated. Representative examples are given in Fig. 7 which
 421 shows relative signal power (averaged over a minute) for all the links involving the HF
 422 receiver at Jicamarca. Noise and, to the greatest extent possible, interference have been
 423 removed from these estimates prior to summing the power in all range and Doppler bins
 424 into which the first-hop signals fell.

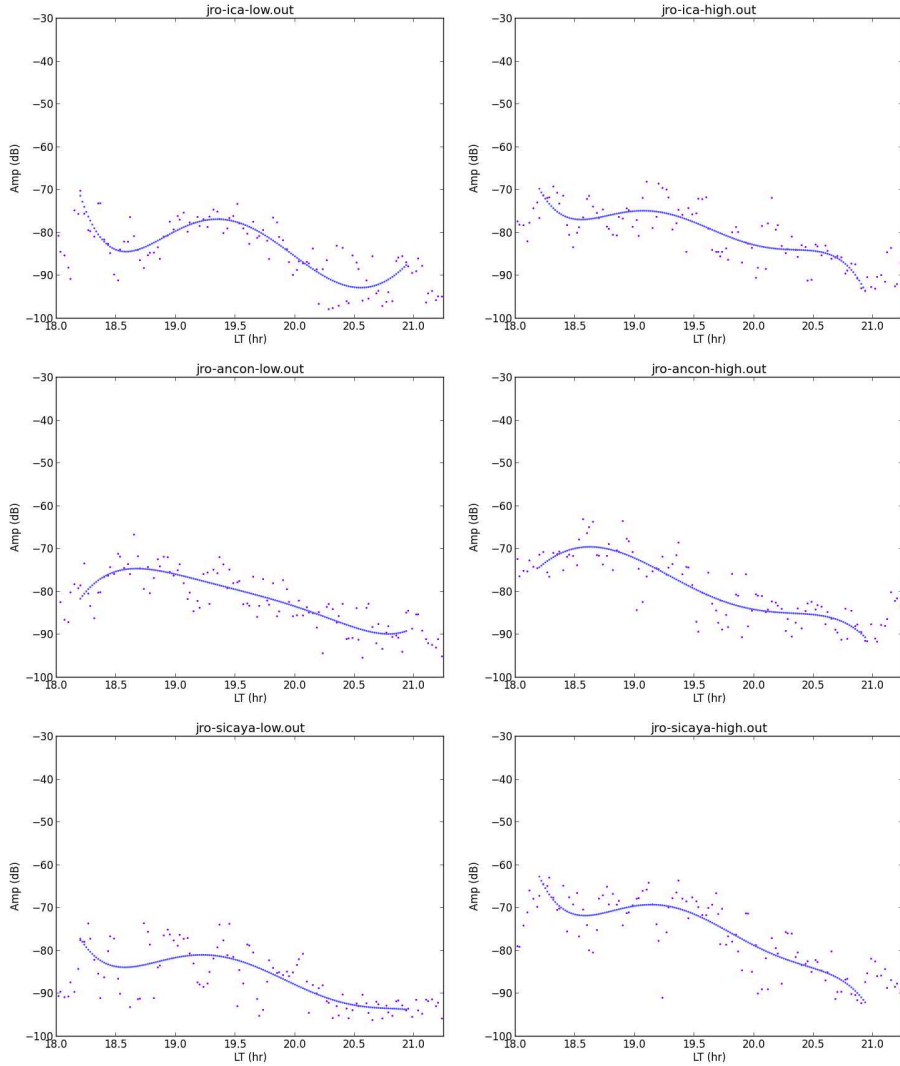


Figure 7. Relative received signal power estimates for the Jicamarca receiver on Dec. 3, 2020.

Smoothed fits to the data are used for subsequent analysis.

425 The signals exhibit considerable small-scale variability or fading which is superim-
 426 posed on large-scale, gradual arcs. Fading at medium and high frequencies has been in-
 427 vestigated since the early days of radio — see Salaman (1962); Davies (1965); Rao et al.
 428 (2002); Bianchi et al. (2013) and references therein for reviews. The causes of fading in-
 429 clude time-variations in absorption and focusing as discussed above. Closely related to
 430 focusing is multipath propagation. Magneto-ionic effects can also cause fading, specif-
 431 ically when the X and O modes are mixed, leading to Faraday rotation and the possi-
 432 bility of time-varying polarization mismatch with linearly-polarized antennas used for
 433 reception.

434 Multipath and polarization fading at HF normally exhibits timescales of a few sec-
 435 onds or less and so should not contribute significantly to the power measurements used
 436 here. Focusing and absorption, meanwhile, should contribute mainly to fading with timescales
 437 of tens of minutes or more. It is these phenomena about which inferences will be made.

438 Finally, scintillation can also cause fading. While the purpose of this investigation
 439 is to characterize the *F* region ionosphere before the onset of ESF and the attendant scin-
 440 tillations, plasma density irregularities are ever present in the equatorial electrojet, and
 441 HF signals have been shown to be strongly affected by them, particularly during the day
 442 but also at night (Woodman et al., 2006). The Fresnel scale for HF signals in the *E* re-
 443 gion is of the order of 2 km which is comparable to the wavelength of large-scale gradi-
 444 ent drift waves in the electrojet (Kudeki et al., 1982). The periods of these waves is tens
 445 to hundreds of seconds. Scintillations likely contribute significantly to the small-scale fad-
 446 ing in the HF data.

447 To incorporate the HF power observables in the analysis, we represent them with
 448 a fifth-degree polynomial fit calculated over the analysis period, 1815–2045 LT in this
 449 case. The fit curves show power levels that peak broadly between about 1830–1930 and
 450 that decrease thereafter. The curve shapes differ between the two HF frequencies and
 451 from station to station, with peaks occurring earlier in the signals from Ancon than in
 452 those from Ica and Sicaya. This would seem to indicate spatial variations in the *F* layer
 453 morphology/curvature.

454 Note that variational sensitivity analysis can be problematic when caustics emerge
 455 in the model N_e field. Caustic isosurfaces are ellipsoidal cylinders aligned with the ray
 456 path. When they emerge, the sensitivity terms go to zero, and iteration over ray bear-

457 ing may stop prematurely. We have found that the problem can be remedied by revert-
 458 ing to brute-force (finite difference) sensitivity analysis on the occasions when conver-
 459 gence fails. Finite differencing dislocates the pilot rays from the small caustic surfaces
 460 sufficiently for convergence to occur.

461 Fig. 8 shows reconstructed electron density isosurfaces from Dec. 3, 2019, between
 462 1845–2000 LT. The bottomside *F* region was evidently steeper on this date than on June
 463 10, 2019, and ascended much more gradually. There is no indication in the Dec. 3, 2019,
 464 isosurfaces of large-scale bottomside perturbations especially conducive to interchange
 465 instability. The relatively steep bottomside combined with the period of plasma ascent
 466 detected by the Jicamarca ISR prior to 2130 therefore remain the most plausible expla-
 467 nations for the modest plumes that erupted eventually from the bottomside scattering
 468 layer seen in Fig. 6.

469 The most important aspect of the isosurfaces in Fig. 8 is their changing curvature.
 470 The isosurfaces went from being slightly concave at 1845 LT to significantly concave be-
 471 tween 1900–1915 LT to nearly flat again at 1930 LT to convex thereafter. The curvature
 472 changes together with the gradual ascent of the *F* layer are broadly consistent with the
 473 relative power levels shown in Fig 7 which peaked early in the event (at different times
 474 for different ray paths) and then decreased as time progressed.

475 In this analysis of postsunset data, the modeled peak *D*-region density was esti-
 476 mated to be fairly uniform and very small, between $5\text{--}10 \times 10^8 \text{ m}^{-3}$ mainly, and too small
 477 to contribute significantly to absorption. Daytime beacon experiments are generally pre-
 478 cluded at Jicamarca by reflection and scattering from the *E* region, and there is only a
 479 small postsunset window when the *D* region can be an important factor in the ray power
 480 budget. Data from within this window were not available in the present dataset. Future
 481 experiments will target the estimation of *D*-region densities before the *D* region has re-
 482 combined.

483 4 Analysis

484 Postsunset ESF is rare during June solstice in the Peruvian sector but occurred (al-
 485beit well after sunset) on June 10, 2019, when the HF high-band pseudorange data also
 486 exhibited unusually distinct quasiperiodic fluctuations. The event was characterized by
 487 a large-scale zonal deformation in the *F*-layer height which appeared to advect eastward

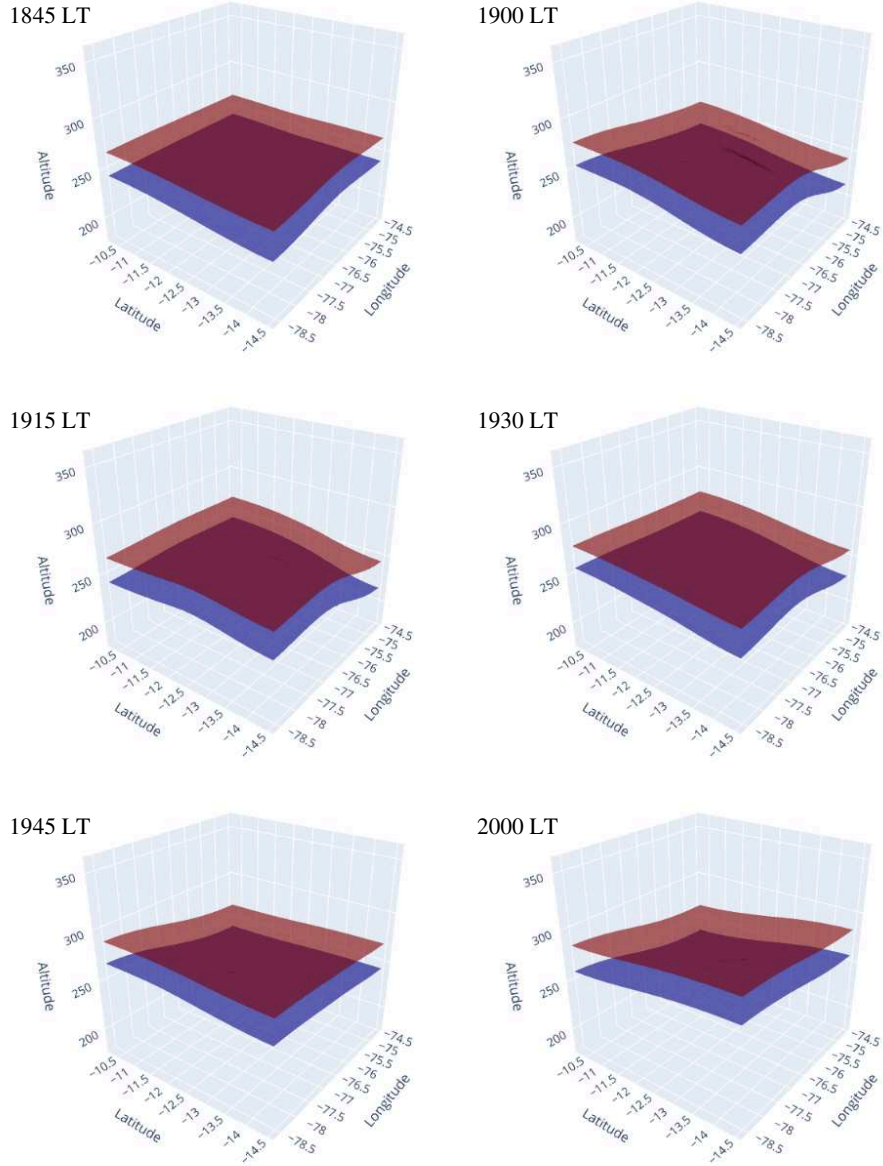


Figure 8. Reconstructed electron density isosurfaces generated from HF pseudorange, Doppler-shift, and power data over a period of 75 min. on Dec. 3, 2019. The blue (red) surfaces represent $N_e = 1 \times 10^{10}$ and $1 \times 10^{11} \text{ m}^{-3}$, respectively.

gradually throughout the event. The horizontal scale of the perturbation was at least several hundred kilometers which is too large to be a direct result of collisional interchange instability (Zargham & Seyler, 1987). A more likely explanation for the structuring is neutral atmospheric forcing which encompasses these scales. The ionospheric deformation indicated in Fig. 2 was significant, with the crest of the deformation being about 100 km higher than the trough. Deformation affects ionospheric stability, the interchange instability growth rate increasing universally with altitude and with decreasing ion-neutral collisions. Depletion plumes would have been more likely to form at the crests of deformations. The morphology of the coherent scatter in Fig. 5 is consistent with this scenario for ESF formation.

In addition, periodic fine structure with a horizontal wavelength of approximately 100 km was superimposed on the large-scale structuring. The fine structure was static rather than propagating and waxed and waned in amplitude with a 30 min. period. While the ionospheric interchange instability can operate at 100-km wavelengths, and while waves can be stationary in the bottomside where the zonal flow exhibits strong shear, periodic amplitude variations suggest a different root cause. Hysell et al. (2014) simulated the response of the equatorial ionosphere to thermospheric waves propagating upward from turbulent regions in the mesosphere with horizontal wavelengths of about 100 km. The waves drove undulations in the bottomside ionization that also waxed and waned with the gravity wave period. As the neutral waves could not remain in phase with the bottomside undulations, the effect was for the former to repeatedly create and destroy the latter. The ionospheric interchange instability was not seeded by the gravity waves in simulation in this case. We do not know what role the file structure played in the occurrence of ESF on June 10, 2019.

Postsunset ESF is climatologically more likely to occur in December solstice than June solstice, and the modest ESF event observed on Dec. 3, 2019, was neither unusual nor anomalous, particularly in view of the small but finite vertical plasma drifts that occurred late in the event. A numerical simulation (not shown) of the event conducted in the manner of Hysell et al. (2015) using ISR data alone predicted the emergence of small depletion plumes late in the event before midnight. Data from the HF network would not have improved the fidelity of that forecast.

519 The most significant finding from the Dec. 3, 2019, HF experiments is that signal
 520 power measurements are broadly consistent with and can be used to help constrain the
 521 morphology/ curvature of the bottomside *F* region. Utilizing all available observables
 522 is important in view of the fact that the recovery problem is strongly underdetermined.
 523 Moreover, the *D*-region density recovered from the analysis was plausible and stable. Fu-
 524 ture experiments spanning twilight and sunset will be necessary to validate the method-
 525 ology going forward.

526 5 Conclusions

527 HF datasets from June and December solstice during very low solar flux conditions
 528 were analyzed using a constrained optimization method to estimate the ionospheric elec-
 529 tron number density regionally in 3D. The method incorporates the HF observables (pseu-
 530 dorange, beat carrier phase, and signal power) as well as data from GPS receivers, an
 531 ionosonde, and the Jicamarca incoherent scatter radar when those data are available.
 532 The regional electron density estimate is initialized shortly after sunset when the *F* re-
 533 gion ionosphere is typically nearly horizontally uniform. Thereafter, the estimate is up-
 534 dated once per minute.

535 Sensitivity analysis using direct variational methods was added to the recovery al-
 536 gorithm. Sensitivity analysis improves stability overall and permits the interpretation
 537 of HF signal power as an additional observable. The signal power is indicative of both
 538 the bottomside *F* region morphology and of absorption along the ray paths. Measuring
 539 it therefore helps the recovery problem, which is strongly underdetermined, and offers
 540 a means of measuring ionization below the *F* layer which can contribute to absorption
 541 before sunset. Note that *D*- and *E*-region density profiles cannot be measured at Jica-
 542 marca due to clutter from irregularities in the mesosphere and the electrojet. Variational
 543 sensitivity analysis can fail when caustics occur in the model ionosphere. In such cases,
 544 a fallback method employing brute-force (finite difference) sensitivity analysis proves to
 545 be more robust.

546 On both occasions considered, modest ESF events characterized by small radar plumes
 547 were observed well after sunset. Traditional forecasts using direct numerical simulations
 548 based solely on incoherent scatter measurements at zenith would not have predicted ESF
 549 in the June 10, 2019, event light of the absence of significant postsunset uplift. The an-

550 alized HF data point to a large-scale background electron density deformation that would
 551 have been difficult to infer from a vertical-pointing ISR and that presumably contributed
 552 to instability. The goal of this work is to learn to make inferences from the HF data that
 553 can be used to inform DNS forecasts and predict ESF in the future.

554 The HF beacon sites are distributed geographically according to the availability
 555 of ground sites. The distribution affects the spatial resolution of the ionospheric recov-
 556 ery. Fine structure at the scale of approximately 100 km can be recovered by the exist-
 557 ing network. This extends into the range of wavelengths at which the ionospheric inter-
 558 change instability operates, meaning that the HF data can be used not only to initial-
 559 ize and constrain the background conditions for DNS simulations but also to seed them.

560 It would be straightforward to use ionospheric recoveries like those in by Figs. 2
 561 and 8 to initialize 3D DNS simulations of ESF. This would be superior to the approach
 562 followed now by Hysell et al. (2015) which is to initialize them using empirical and physics-
 563 based models tuned to match Jicamarca observations assuming an equivalence between
 564 local time and longitude. A more comprehensive approach to simulation would be to as-
 565 similate the HF data directly. While we plan to attempt this, the computational cost
 566 is likely to be quite high based on our experience with the comparatively simple constrained
 567 optimization problem being solved presently. A third option which seems promising for
 568 real-time forecasting is machine learning based on complementary HF and ISR data. This
 569 approach should be explored as well once a dataset large enough for training has been
 570 assembled.

571 **Appendix A Direct variational sensitivity analysis**

572 Here, we provide details regarding sensitivity analysis in the raytracing method-
 573 ology. The analysis begins with the augmentation of the equations used for updating the
 574 raytracing state vector. The state vector includes the coordinates and their conjugate
 575 momenta at points defining the ray, i.e. in spherical coordinates, $p = (k_r, k_\theta, k_\phi, r, \theta, \phi)$.
 576 Other parameters may be added to the state vector, for example the phase path length
 577 and power, but only these six are required for raytracing.

578 The raytracing equations are Hamilton's equations for the Hamiltonian $H(p, \omega, t)$.
 579 They can be derived from the Euler Lagrange equations and the application of variational
 580 mechanics to Fermat's principle. The result is a system of coupled differential equations

581 of the form (see Eqns. (9)–(14) in Jones and Stephenson (1975)):

$$p'_i = f_{1i}(r, \theta) \frac{1}{c} \frac{H_{p_j}}{H_\omega} + f_{2i}(r, \theta, k_\theta, k_\phi, p') \quad (A1)$$

582 where $p'_i \equiv dp_i/dP$, $P = ct$ is the group path length, $H_{p_j} \equiv \partial H/\partial p_j$ and $H_\omega \equiv \partial H/\partial \omega$
 583 denote components of the gradient of the Hamiltonian, and where f_{1i} and f_{2i} arise from
 584 the metric tensor for spherical coordinates. Also, p_i is conjugate to p_j . The Hamiltonian
 585 is based on an invariant quantity along a ray path and can be expressed in a number of
 586 ways (see below). For the present purposes, the Hamiltonian is taken to be time invariant-
 587 ant. At every step, the equations are solved using numerical quadrature.

588 The corresponding equations describing the sensitivity of the state vector to a control
 589 parameter λ therefore take the form (noting that the prime and the $\partial/\partial\lambda$ operators
 590 may be interchanged):

$$\begin{aligned} & \left(\frac{\partial p_i}{\partial \lambda} \right)' \\ &= f_{1i}(r, \theta) \frac{1}{c} \frac{\{H_{p_j}, H_\omega\}}{H_\omega^2} + \left(\frac{1}{c} \frac{H_{p_j}}{H_\omega} \frac{\partial f_{1i}}{\partial p_k} + \frac{\partial f_{2i}}{\partial p_k} \right) \frac{\partial p_k}{\partial \lambda} + \frac{\partial f_{2i}}{\partial p'_k} \frac{\partial p'_k}{\partial \lambda} \end{aligned} \quad (A2)$$

591 where we employ the notation

$$\{H_{p_j}, H_\omega\} \equiv (H_\omega H_{p_j, p_k} - H_{p_j} H_{\omega, p_k}) \frac{\partial p_k}{\partial \lambda}, \quad (A3)$$

592 where H_{p_j, p_k} and H_{ω, p_k} denote components of the Hessian of the Hamiltonian, and where
 593 the Einstein summation convention is used throughout. Note that the six equations have
 594 the same form for any control parameter. The difference lies just in the initial conditions
 595 for $\partial p_i/\partial\lambda$. Using the ray bearing as control parameters, for example, the initial con-
 596 ditions are just the derivatives of the initial wavevector with respect to azimuth and el-
 597 evation with wavenumber held constant.

598 The new equations augment the original ones and are evaluated in the same nu-
 599 matical quadrature, only now with six additional equations per control parameter. Each
 600 equation like Eq. A2 contains terms on the right side of the form $\partial p_k/\partial\lambda$ which are avail-
 601 able for computation, having been evaluated through numerical quadrature up through
 602 the current point on the ray. Since f_{2i} may contain p' , there may be additional terms
 603 of the form $(\partial p_k/\partial\lambda)'$ on the right side of Eq. A2 as well. However, such terms appear
 604 only in the sensitivity equations for the momenta (k_r, k_θ, k_ϕ) and involve only the co-
 605 ordinates (r, θ, ϕ) . If the sensitivities for the coordinates are calculated first at each point
 606 on the ray, the information required for the momenta sensitivities, which are calculated
 607 next, will be available explicitly.

608 The Hamiltonian used for calculations here is the dispersion relation for the waves:

$$H = \Re \left\{ \frac{1}{2} \left(\frac{c^2 k^2}{\omega^2} - n^2(p, \omega) \right) \right\}$$

609 The gradient and Hessian of the Hamiltonian can be calculated readily from the gradi-
610 ent and Hessian of the square of the index of refraction. For the latter, we utilize the Ap-
611 pleton Hartree equation:

$$n^2(X, Y_l, Y_t, Z) = \frac{1 - iZ - X}{2(1 - iZ)(1 - iZ - X) - Y_t^2 \pm \sqrt{Y_t^4 + 4Y_l^2(1 - iZ - X)^2}} \quad (A4)$$

612 in which the \pm sign distinguishes between the ordinary and extraordinary mode. This
613 formula is posed compactly in terms of the magneto-ionic parameters $X \equiv \omega_p^2/\omega^2$, $Y \equiv$
614 Ω_e/ω , and $Z \equiv \nu_{en}/\omega$. Furthermore, we have the longitudinal and transverse compo-
615 nents

$$\begin{aligned} Y_l &\equiv Y \hat{k} \cdot \hat{b} \\ Y_t &\equiv \sqrt{Y^2 - Y_l^2} \end{aligned}$$

616 The gradients and Hessians of Eq. A4 in terms of the four magneto-ionic parameters are
617 somewhat involved but can be calculated expediently with the aid of computer algebra.

618 The $X(r, \theta, \phi)$ parameter contains the spatial dependence on electron-density that
619 is central to the experimental method. The most complicated parameters are $Y_t(p)$ and
620 $Y_l(p)$ which introduce anisotropy into the problem and which depend both on the wavevec-
621 tor and on the magnitude and direction of the magnetic field. The Z dependence con-
622 tains electron-neutral collisions which render a prediction of absorption. We take $Z =$
623 $Z(r)$ here to simplify the calculations, presupposing no knowledge about the horizon-
624 tal distribution of neutral pressure controlling the electron-neutral collision frequency.

625 Defining the magneto-ionic state vector $s \in (X, Y_l, Y_t, Z)$, we have the transfor-
626 mations

$$n_{p_i}^2 = n_{s_k}^2 s_{k,p_i} \quad (A5)$$

$$n_{p_i, p_j}^2 = n_{s_k, s_l}^2 s_{k,p_i} s_{l,p_j} + n_{s_k}^2 s_{k,p_i, p_j} \quad (A6)$$

627 In this way, the gradient and Hessian of the square of the index of refraction are related
628 to the gradient and Hessian of the magneto-ionic parameters. Calculating the various
629 terms that enter into eqs. A5–A6 is regrettably tedious. Computer algebra can simplify
630 the calculations considerably here as well.

631 The plasma number density profile $n_e(r) = n_e(R_e+h)$ is parameterized in the ver-
 632 tical in terms of either Chapman functions or semi-Epstein functions as described above.
 633 In either case, five parameters control the shape of the profile. Each of the five param-
 634 eters is expanded in a bicubic B-spline basis spanning the range of colatitudes and lon-
 635 gitudes included in the model space, i.e. $d1 \cdots d5 = d1(\theta, \phi) \cdots d5(\theta, \phi)$. The gradient
 636 and Hessian of the magneto-ionic parameter X in terms of the ray parameters p then
 637 become:

$$X_r/a = n_{e,h} \quad (A7)$$

$$X_{r,r}/a = n_{e,h,h} \quad (A8)$$

$$X_{r,\theta}/a = n_{e,h,d_k} d_{k,\theta} \quad X_{r,\phi}/a = n_{e,h,d_k} d_{k,\phi} \quad (A9)$$

$$X_{\theta}/a = n_{e,d_k} d_{k,\theta} \quad X_{\phi}/a = n_{e,d_k} d_{k,\phi} \quad (A10)$$

$$X_{\theta,\theta}/a = n_{e,d_k,d_l} d_{k,\theta} d_{l,\theta} + n_{e,d_k} d_{k,\theta,\theta} \quad (A11)$$

$$X_{\theta,\phi}/a = n_{e,d_k,d_l} d_{k,\theta} d_{l,\phi} + n_{e,d_k} d_{k,\theta,\phi} \quad (A12)$$

$$X_{\phi,\phi}/a = n_{e,d_k,d_l} d_{k,\phi} d_{l,\phi} + n_{e,d_k} d_{k,\phi,\phi} \quad (A13)$$

638 where the constant $a \equiv e^2/\epsilon m_e \omega$. Here again, the gradients and Hessians of n_e are most
 639 easily computed with the aid of computer algebra. The $d_k(\theta, \phi)$ parameters are polyno-
 640 mial functions, and the corresponding gradients and Hessians are themselves straight-
 641 forward to calculate.

642 The Y_t and Y_l gradients and Hessians are calculated in part with the help of the
 643 IGRF-20 magnetic field model. The terms that involve purely spatial derivatives are cal-
 644 culated entirely using finite differences with a 19-point stencil. The terms that involve
 645 purely wavenumber derivatives are calculated strictly analytically. Cross-derivative Hes-
 646 sian terms involving both spatial and wavenumber gradients are computed with a hy-
 647 brid approach. Wavenumber gradients are computed analytically, and spatial gradients
 648 are computed using finite differences. The spatial gradients of the magnetic field used
 649 to calculate Y are computed using the same stencil referenced above.

650 Insofar as the calculation of the gradient and Hessian of Y_t , the purely spatial com-
 651 ponents are computed with finite differences as with Y_l . For the remaining terms, it is
 652 expedient to begin with the results for Y_l and apply the following transformations:

$$Y_{t,p_i} = \frac{1}{Y_t} (YY_{p_i} - Y_l Y_{l,p_i})$$

$$Y_{t,p_i,p_j} = \frac{1}{Y_t} (Y_{p_i} Y_{p_j} + YY_{p_i p_j} - Y_{l,p_i} Y_{l,p_j} - Y_l Y_{l,p_i,p_j} - Y_{t,p_i} Y_{t,p_j})$$

653 where we note that the wavenumber derivatives of Y and therefore the cross-derivative
 654 terms $Y_{p_i} Y_{p_j}$ involving wavenumber derivatives are zero.

655 Finally, the Z parameter depends only on the range r , and its first and second deriva-
 656 tives with respect to r are trivial for the case of the bi-exponential effective electron-neutral
 657 collision frequency profile considered here.

658 **Acknowledgments**

659 This work was supported by award FA9550-12-1-0462 from the Air Force Office of
 660 Scientific Research and by DARPA under Department of the Interior D19AC00009 to
 661 the Georgia Institute of Technology with subaward to Cornell University. The Jicamarca
 662 Radio Observatory is a facility of the Instituto Geofísico del Perú operated with support
 663 from NSF award AGS-1732209 through Cornell. The help of the staff is much appreci-
 664 ated. Data used for this publication are available through the Madrigal database (see
 665 <http://www.openmadrigal.org.>)

666 **References**

667 Abdu, M. A., Kherani, E. A., Batista, I. S., de Paula, E. R., & Fritts, D. C. (2009).
 668 An evaluation of the ESF/bubble irregularity growth conditions under gravity
 669 wave influences based on observational data from the SpreadFEx campaign.
 670 *Ann. Geophys.*, 27, 2607.

671 Aveiro, H. C., Hysell, D. L., Park, J., & Luhr, H. (2011). Equatorial spread F-
 672 related currents: Three-dimensional simulations and observations. *Geophys.*
 673 *Res. Lett.*, 38, L21103.

674 Bartholomew-Biggs, M., Brown, S., Christianson, B., & Dixon, L. (2000). Auto-
 675 matic differentiation of algorithms. *J. Comp. Appl. Math.*, 124(1–2), 171–190,
 676 [https://doi.org/10.1016/S0377-0427\(00\)00422-2](https://doi.org/10.1016/S0377-0427(00)00422-2).

677 Bianchi, C., Baskaradas, J. A., Pezzopane, M., Pietrella, M., Sciacca, U., & Zuc-
 678 cheretti, E. (2013). Fading in the HF ionospheric channel and the role of
 679 irregularities. *Adv. Space Res.*, 52, 403–411.

680 Booker, H. G., & Wells, H. W. (1938). Scattering of radio waves by the F region.
 681 *Terres. Magn.*, 43, 249.

682 Bourne, H. (2016). *Algorithm for accurate ionospheric total electron content and*

683 receiver bias estimation using GPS measurements. MS Thesis, Colorado State
 684 University.

685 Bourne, H., Morton, Y., van Graas, F., Sulzer, M., & Milla, M. (2016). *Spacial*
 686 *gradient based TEC estimation algorithm with code noise multipath correc-*
 687 *tion evaluation using simultaneous incoherent scatter radar measurements.*
 688 Proceedings of the 2016 International Technical Meeting of The Institute of
 689 Navigation, Monterey, California, January 2016, pp. 140-150.

690 Budden, K. G. (1985). *The propagation of radio waves*. New York: Cambridge Univ.
 691 Press.

692 Budden, K. G. (1991). Ray tracing and the effect of ray divergence and convergence
 693 on signal amplitude. *Proc. R. Soc. London A*, *432*, 233–246.

694 Cacuci, D. G., Weber, C. F., Oblow, E. M., & Marable, H. (1980). Sensitivity theory
 695 for general systems of nonlinear equations. *Nuc. Sci. Eng.*, 88–110.

696 Cao, Y., Li, S., Petzold, L., & Serban, R. (2003). Adjoint sensitivity analysis for dif-
 697 ferential algebraic equations. *J. Sci. Comput.*, *23*(3), 1076–1089.

698 Chau, J. L., & Woodman, R. F. (2001). Interferometric and dual beam observations
 699 of daytime spread-*F*-like irregularities over Jicamarca. *Geophys. Res. Lett.*, *28*,
 700 3581.

701 Coleman, C. J. (2011). Point-to-point ionospheric ray tracing by a direct variational
 702 method. *Radio Sci.*, *46*(RS5016), doi:10.1029/2011RS004748.

703 Cummer, S. A., Inan, U. S., & Bell, T. F. (1998). Ionospheric *D* region remote sens-
 704 ing using VLF radio atmospherics. *Radio Sci.*, *33*(6), 1781–1792.

705 Davies, K. (1965). *Ionospheric radio propagation* (No. 80). Washington, D.C.: Na-
 706 tional Bureau of Standards Monograph, U.S. Govt. Printing Office.

707 De-Boor, C. (1978). *A practical guide to splines*. New York: Springer Verlag.

708 Farley, D. T., Balsley, B. B., Woodman, R. F., & McClure, J. P. (1970). Equatorial
 709 spread *F*: Implications of VHF radar observations. *J. Geophys. Res.*, *75*, 7199.

710 Hairer, E., & Wanner, G. (1990). *Solving ordinary differential equations ii. Stiff and*
 711 *differential-algebraic problems*. Springer-Verlag.

712 Huang, C. S., Kelley, M. C., & Hysell, D. L. (1994). Nonlinear Rayleigh-Taylor
 713 instabilities, atmospheric gravity waves, and equatorial spread *F*. *J. Geophys.*
 714 *Res.*, *98*, 15,631.

715 Hwang, J., Dougherty, E., Rabitz, S., & Rabitz, H. (1978, 12). The Green's func-

716 tion method of sensitivity analysis in chemical kinetics. *The Journal of Chemical*
717 *Physics*, 69, 5180-5191. doi: 10.1063/1.436465

718 Hysell, D. L., Baumgarten, Y., Milla, M. A., Valdez, A., & Kuyeng, K. (2018).
719 Ionospheric specification and space weather forecasting with an HF bea-
720 con network in the Peruvian sector. *J. Geophys. Res.*, 123, 6851–6864,
721 <https://doi.org/10.1029/2018JA025648>.

722 Hysell, D. L., & Chau, J. L. (2001). Inferring *E* region electron density profiles at Ji-
723 camarca from Faraday rotation of coherent scatter. *J. Geophys. Res.*, 106, doi:
724 10.1029/2000JA001101.

725 Hysell, D. L., Jafari, R., Milla, M. A., & Meriwether, J. W. (2014). Data-driven nu-
726 merical simulations of equatorial spread *F* in the Peruvian sector. *J. Geophys.*
727 *Res.*, doi:10.1002/2014JA019889.

728 Hysell, D. L., Milla, M. A., Condori, L., & Vierinen, J. (2015). Data-driven nu-
729 merical simulations of equatorial spread *F* in the Peruvian sector 3: Solstice. *J.*
730 *Geophys. Res.*, 120, 10,809–10,822, doi:10.1002/2015JA021877.

731 Hysell, D. L., Rao, S., Groves, K. M., & Larsen, M. F. (2020). Radar investigation
732 of postsunset equatorial ionospheric stability over Kwajalein during project
733 WINDY. *J. Geophys. Res.*, <https://doi.org/10.1029/2020ja027997>.

734 Jones, R. M., & Stephenson, J. J. (1975). *A versatile three-dimensional ray tracing*
735 *computer program for radio waves in the ionosphere* (Tech. Rep. No. 75-76).
736 Washington, D.C.: U. S. Department of Commerce.

737 Kelley, M. C., Larsen, M. F., & La Hoz, C. (1981). Gravity wave interaction of equa-
738 torial spread *F*: A case study. *J. Geophys. Res.*, 86, 9087.

739 Keskinen, M. J., Ossakow, S. L., & Chaturvedi, P. K. (1980). Preliminary report of
740 numerical simulations of intermediate wavelength collisional Rayleigh-Taylor
741 instability in equatorial spread *F*. *J. Geophys. Res.*, 85, 1775.

742 Keskinen, M. J., & Vadas, S. L. (2009). Three-dimensional nonlinear evolution
743 of equatorial ionospheric bubbles with gravity wave seeding and tidal wind
744 effects. *Geophys. Res. Lett.*, 36, L12102, doi:10.1029/2009GL037892.

745 Krall, J., Huba, J. D., & Fritts, D. C. (2013). On the seeding of equato-
746 rial spread *F* by gravity waves. *Geophys. Res. Lett.*, 40(4), 661–664,
747 doi:10.1002/GRL.50144.

748 Krall, J., Huba, J. D., Joyce, G., & Zalesak, T. (2009). Three-dimensional simu-

749 lation of equatorial spread-F with meridional wind effects. *Ann Geophys.*, *27*,
 750 1821–1830.

751 Kudeki, E., Farley, D. T., & Fejer, B. G. (1982). Long wavelength irregularities in
 752 the equatorial electrojet. *Geophys. Res. Lett.*, *9*, 684.

753 Landau, L. D., & Lifshitz, E. M. (1976). *Mechanics* (Third edition ed.). Elsevier.

754 McCormick, J. C. (2019). *D region tomography: A technique for ionospheric imaging*
 755 *using lightning-generated sferics and inverse modeling* (Unpublished doctoral
 756 dissertation). Georgia Technical Institute.

757 Nava, B., Coisson, P., & Radicella, S. M. (2008). A new version of the NeQuick
 758 ionosphere electron density model. *J. Atmos. Sol. Terr. Phys.*, *70*, 1856–1862.

759 Nickisch, L. J. (1988). Focusing in the stationary phase approximation. *Radio Sci.*,
 760 *23*(2), 171–182.

761 Ossakow, S. L. (1981). Spread *F* theories – A review. *J. Atmos. Terr. Phys.*, *43*,
 762 437.

763 Psiaki, M. (2019). Ionosphere ray tracing of radio-frequency signals and
 764 solution sensitivities to model parameters. *Radio Sci.*, *54*, 738–757,
 765 <https://doi.org/10.1029/2019RS006792>.

766 Psiaki, M. L., Bust, G. S., & Mitchell, C. N. (2015). Nonlinear estimation to as-
 767 similate GPS TEC data into a regional ionosphere model. *Proc. ION GNSS+*
 768 *2015*, 34973510.

769 Rao, S. V. B., Rao, T. R., Reddy, V. G., Lakshmi, D. R., Veenadhari, B., Dabas,
 770 R. S., ... Reddy, B. M. (2002). HF radio signal fading and atmo-
 771 spheric radio noise measurements at low latitudes. *Radio Sci.*, *37*(5),
 772 doi:10.1029/2001RS002495.

773 Röttger, J. (1981). Equatorial spread *F* by electric fields and atmospheric gravity
 774 waves generated by thunderstorms. *J. Atmos. Terr. Phys.*, *43*, 453.

775 Salaman, R. K. (1962). *Historical survey of fading at medium and high frequencies*
 776 (Tech. Rep. No. 133). Washington, D.C.: National Bureau of Standards.

777 Sambridge, M. S., & Kennett, B. L. N. (1990). Boundary value ray tracing in a het-
 778 erogeneous medium: a simple and versatile algorithm. *Geophys. J. Int.*, *101*,
 779 157–168.

780 Schunk, R., & Nagy, A. (2009). *Ionospheres: Physics, plasma physics, and chemistry*
 781 (2nd ed.). Cambridge University Press.

782 Sen, H. K., & Wyller, A. A. (1960). On the generalization of the Appleton-Hartree
783 magnetoionic formulas. *J. Geophys. Res.*, *65*, 3931–3950.

784 Settimi, A., Pietrella, M., Pezzopane, M., & Bianchi, C. (2015). The IONORT-ISP-
785 WC system: Inclusion of an electron collision frequency model for the D-layer.
786 *Adv. Space Res.*, *55*, 2114–2123.

787 Singh, S., Johnson, F. S., & Power, R. A. (1997). Gravity wave seeding of equatorial
788 plasma bubbles. *J. Geophys. Res.*, *102*, 7399.

789 Taori, A., Patra, A. K., & Joshi, L. M. (2011). Gravity wave seeding of equa-
790 torial plasma bubbles: An investigation with simultaneous F-region, E-
791 region, and middle atmospheric measurements. *J. Geophys. Res.*, *116*,
792 doi:10.1029/2011JA016229.

793 Tromp, J., Tape, C., & Liu, Q. (2005). Seismic tomography, adjoint methods, time
794 reversal and banana-doughnut kernels. *Geophys. J. Int.*, *195*–216.

795 Tsunoda, R. T. (2010). On seeding equatorial spread F: Circular gravity waves.
796 *Geophys. Res. Lett.*, *37*, L10104, doi:10.1029/2010GL043422.

797 Tsunoda, R. T., Barons, M. J., Owen, J., & Towle, D. M. (1979). Altair: An inco-
798 herent scatter radar for equatorial spread *F* studies. *Radio Sci.*, *14*, 1111.

799 Tsunoda, R. T., Bubenik, D. M., Thampi, S. V., & Yamamoto, M. (2010). On large-
800 scale wave structure and equatorial spread *F* without a post-sunset rise of the
801 *F* layer. *Geophys. Res. Lett.*, *37*, L07105, doi:10.1029/2009GL042357.

802 Västberg, A., & Lundborg, B. (1996). Signal intensity in the geometric optics ap-
803 proximation for the magnetized ionosphere. *Radio Sci.*, *31*(6), 1579–1588.

804 Woodman, R. F., Chau, J. L., & Ilma, R. R. (2006). Comparison of ionosonde and
805 incoherent scatter drift measurements at the magnetic equator. *Geophys. Res.*
806 *Lett.*, *33*(L01103), doi:10.1029/2005GL023692.

807 Woodman, R. F., & La Hoz, C. (1976). Radar observations of *F* region equatorial ir-
808 regularities. *J. Geophys. Res.*, *81*, 5447–5466.

809 Yokoyama, T., Shinagawa, H., & Jin, H. (2014, 12). Nonlinear growth, bifurcation
810 and pinching of equatorial plasma bubble simulated by three-dimensional high-
811 resolution bubble model. *Journal of Geophysical Research: Space Physics*, *119*,
812 10,474–10,482.

813 Zalesak, S. T., Drake, J. F., & Huba, J. D. (1990). Three-dimensional simulation
814 study of ionospheric plasma clouds. *Geophys. Res. Lett.*, *17* (10), 1597–1600.

815 Zalesak, S. T., Ossakow, S. L., & Chaturvedi, P. K. (1982). Nonlinear equatorial
816 spread F - The effect of neutral winds and background Pedersen conductivity.
817 *J. Geophys. Res.*, 87, 151–166.

818 Zargham, S., & Seyler, C. E. (1987). Collisional interchange instability, 1, Numerical
819 simulations of intermediate-scale irregularities. *J. Geophys. Res.*, 92, 10,073.

820 Zargham, S., & Seyler, C. E. (1989). Collisional and inertial dynamics of the iono-
821 spheric interchange instability. *J. Geophys. Res.*, 94, 9009.

822 Zawdie, K. A., Drob, D. P., Siskind, D. E., & Coker, C. (2017). Calculating the
823 absorption of HF radio waves in the ionosphere. *Radio Sci.*, 52, 767–783,
824 doi:10.1002/2017RS006256.